https://doi.org/10.5194/egusphere-2026-25
Preprint. Discussion started: 27 February 2026

Impacts of synoptic circulation types on nocturnal ozone increase in the North China Plain: Meteorological drivers and formation mechanisms

Huanpeng Wang[1], Liya Fan[1,2,3,4*], Xuejiao Deng[5], Haomin Huang[1,2,3,4], Daiqi Ye[1,2,3,4]

[1]School of Environment and Energy, South China University of Technology, Guangzhou, 510006, China
[2]National Engineering Laboratory for Volatile Organic Compounds Pollution Control Technology and Equipment, Guangzhou, 510006, China
[3]Guangdong Provincial Key Laboratory of Atmospheric Environment and Pollution Control, Guangzhou, 510006, China
[4]Guangdong Provincial Engineering and Technology Research Centre for Environmental Risk Prevention and Emergency Disposal, Guangzhou, 510006, China
[5]Key Laboratory of Regional Numerical Weather Prediction, Guangzhou Institute of Tropical and Marine Meteorology, China Meteorological Administration, Guangzhou, 510680, China

Correspondence to: Liya Fan (fanly@scut.edu.cn)

Abstract. Nocturnal ozone increase (NOI) has become common worldwide, raising the risk of ozone pollution. Weather types serve as one of the critical drivers of NOI, but how they influence NOI remains poorly understood. Using ground observation and reanalysis datasets, this study identified the relationship between weather types and NOI days in a representative city on the North China Plain, and investigated the meteorological characteristics and formation mechanisms of NOI days under different weather types. During 2021-2023, 392-470 NOI days were observed, with the occurrence predominantly concentrated between 00:00 and 06:00 local time (71.35%). Based on the Lamb-Jenkinson method, NOI days were classified into four primary weather types: A-type (57.36%), C-type (11.17%), S-type (20.81%) and WNE-type (10.66%). A-type was dominated by high-pressure anticyclones with mild weather condition, whereas C-type was controlled by low-pressure systems and influenced by moist airflows. S-type was located in the transition zone between high and low pressure, influenced by southern geostrophic winds, and WNE-type was characterized by high-pressure systems with W-N-E geostrophic flows. Notably, under all four weather types, the formation of NOI days was attributed to the synergy of regional and vertical transport. Specifically, under S-type and WNE-type, regional transport was influenced by geostrophic winds, while vertical transport was associated with high-pressure subsidence (A-type and WNE-type), cold pool subsidence (C-type), and shallow convection (S-type). This study elucidates the diverse dynamical pathways of weather-driven NOI, and provides mechanistic insights for improving ozone forecasting and mitigation strategies in urban environments.

1 Introduction

Surface ozone (O_3), a typical secondary pollutant, poses significant risks to human health due to its strong oxidative properties (Paoletti, 2009; Monks et al., 2009). Excessive O_3 can lead to increased incidence and mortality rates of asthma, cardiovascular

https://doi.org/10.5194/egusphere-2026-25
Preprint. Discussion started: 27 February 2026

and respiratory diseases (Liu et al., 2023; Cheng et al., 2022; Gilardi et al., 2023; Zhao et al., 2022). Formed primarily through photochemical reactions of volatile organic compounds (VOCs) and nitrogen oxides (NO_x) under sunlight (Li et al., 2022b; Li et al., 2022a; Wang et al., 2023a), O_3 typically peaks during the daytime and declines at night due to deposition and NO_x titration (Li et al., 2022b; Shen et al., 2024; He et al., 2021; Zhu et al., 2020). In China, despite successful reductions in particulate matter (PM) since the 2013 Air Pollution Prevention and Control Action Plan, O_3 pollution has intensified, particularly in the North China Plain (NCP) (Shen et al., 2024; Xu et al., 2021; Dong et al., 2020; Song et al., 2022). Meanwhile, recent observations in the NCP have revealed an unexpected phenomenon of nocturnal O_3 increase (NOI) (He et al., 2021; Zhu et al., 2020). The occurrence of NOI not only increases nighttime O_3 levels but also poses a potential risk of O_3 pollution on the following day. Previous studies have demonstrated NOI's promoting effect on O_3 pollution (Wang et al., 2025; He et al., 2022; Wang et al., 2023d; Zhu et al., 2020), but the underlying mechanisms and contributing drivers of NOI are not yet fully understood.

NOI events, characterized by unexpected rises in nighttime O_3 concentrations (at least 10 μg m^{-3} per hour (Zhu et al., 2020)), challenge the conventional understanding of O_3 (Wang et al., 2023b; Xue et al., 2023; Chen et al., 2024b). Previously, nocturnal O_3 was often overlooked owing to its low concentrations. However, the occurrence of NOI events can result in a rapid surge in nighttime O_3 levels, with hourly concentrations even surpassing 160 μg m^{-3} (Wang et al., 2023d; Zhu et al., 2024). High concentrations of nocturnal O_3 also have a significant impact on human health and plant growth (Chowdhury et al., 2022; Hoshika et al., 2019). NOI events, usually driven by horizontal and vertical transport processes, are linked to meteorological activities such as sea-land winds (Nair et al., 2002), valley winds (Sánchez et al., 2005; Xue et al., 2023), low-level jets and convective storms (Zhu et al., 2020; Wu et al., 2023). While daytime O_3 pollution is well-documented, NOI remains poorly understood, necessitating the research into its meteorological drivers and formation mechanisms.

Apart from emissions of O_3 precursors, meteorological conditions play a crucial role in O_3 formation (Dong et al., 2020). Weather conditions of high temperature, low humidity, and strong solar radiation are conducive to the photochemical generation of O_3 (Liang et al., 2022; Chen et al., 2024b). The environment of low wind speed and high-pressure often leads to stagnant weather conditions, resulting in localized O_3 accumulation (Liu et al., 2025). These weather conditions are largely determined by local synoptic circulation types (Xu et al., 2021; Song et al., 2022; Chen et al., 2024b). For example, Shen et al. (2024) found that persistent O_3 pollution events over Wuxi from 2014 to 2021 were primarily associated with subtropical high-pressure and weak pressure systems, characterized by dry and hot local weather conditions. Ji et al. (2023) reported that high O_3 concentrations in southeastern coastal areas of China from 2015 to 2020 were mainly linked to high-pressure anticyclonic activity, which frequently occurs in spring. You et al. (2024) observed that O_3 pollution in the Pearl River Delta region during autumn from 2015 to 2021 was often influenced by the Siberian high-pressure system, with significant cross-regional transport from the northeast. These studies highlight the role of weather types in O_3 pollution, yet the specific meteorological drivers of NOI remain underexplored, particularly in rapidly urbanizing regions like the NCP.

Located in the southern NCP, Xinxiang is an industrial and transportation hub bordered by the Taihang Mountain to the north and the Yellow River to the south (Fig. S1). This unique topography, combined with high emissions, makes Xinxiang a critical

https://doi.org/10.5194/egusphere-2026-25
Preprint. Discussion started: 27 February 2026

case study for understanding NOI. This study aims to bridge the gap between synoptic-scale drivers and local NOI occurrences. By integrating three-year (2021-2023) high-frequency observations with the Lamb-Jenkinson method, we (1) investigate the temporal variability characteristics of NOI, (2) identify the dominant synoptic circulation types conducive to NOI, and (3) unravel the distinct physical mechanisms that govern NOI under different weather types. These insights not only enhance our understanding of the nocturnal O_3 budget but also provide a scientific basis for improving O_3 forecasting and mitigation strategies in urban environments.

2 Data and methods

2.1 Data sources

Hourly ground observation data including O_3 concentration, temperature, relative humidity, wind speed, wind direction and precipitation were obtained from four national monitoring stations in Xinxiang (named Development Zone (KF), Environmental Protection East Hospital (DY), Environmental Protection West Court (XY) and Municipal Party School (DX), respectively). The detailed information is shown in Fig. S1. Sea level pressure (SLP) data and 17-layer vertical profiles (500-1000 hPa) of vorticity, wind speed, wind direction, temperature, relative humidity and O_3 concentration were acquired from the Modern-Era Retrospective Analysis for Research and Applications dataset (MERRA-2, Version 2) (https://disc.gsfc.nasa.gov/). This dataset was constructed by NASA Global Modeling and Assimilation Office (GMAO) using the Goddard Earth Observing System (GEOS) assimilation model, and has been widely applied in weather typing studies worldwide (Zhang et al., 2022; Gelaro et al., 2017; Molod et al., 2015; Li et al., 2020b). Additionally, planetary boundary layer height (PBLH), friction velocity (U^*), and convective available potential energy (CAPE) were derived from the ERA5 reanalysis dataset (https://www.ecmwf.int/en/forecasts/dataset/ecmwf-reanalysis-v5) provided by the European Centre for Medium-Range Weather Forecasts (ECMWF), which offers superior boundary layer parameters (Hersbach et al., 2020; Bell et al., 2021).

2.2 Definition of NOI events and NOI days

NOI event is defined as an hourly O_3 concentration increment exceeding 10 μg m^{-3} during nighttime (20:00-06:00 local time, LT; UTC+8, Beijing Time) (He et al., 2021; Zhu et al., 2020). A day is classified as an NOI day if such events occur either during 00:00-06:00 or 20:00-23:00 LT. Based on the occurrence time of NOI, NOI days are categorized into three types: Type A, NOI occurs only between 00:00 and 06:00 LT; Type B, NOI occurs only between 20:00 and 23:00 LT; Type C, NOI occurs both 00:00-06:00 and 20:00-23:00 LT.

2.3 Lamb-Jenkinson synoptic circulation classification approach

The Lamb-Jenkinson synoptic circulation classification approach serves as a precise and efficient meteorological classification method, which has been widely used in many studies (Zhu et al., 2007; Duan et al., 2020; Wu et al., 2020; Wang et al., 2023e).

https://doi.org/10.5194/egusphere-2026-25
Preprint. Discussion started: 27 February 2026

In this study, 16 grid points were selected around Xinxiang in accordance with Lamb-Jenkinson approach. The grid points cover the region from 25°N to 45°N and 100°E to 130°E, with a grid spacing of 5° in latitude and 10° in longitude (Fig. S2). Based on SLP data from the selected grid points, 6 circulation indices were calculated (Zhou et al., 2023; You et al., 2024; Liu et al., 2019). The corresponding calculation formulas and circulation indices are introduced as follows:

$$u=0.5(P12+P13-P4-P5) \quad (1)$$

$$v=\frac{1}{\cos\alpha}\times\frac{1}{4}(P5+2P9+P13-P4+2P8-P12) \quad (2)$$

$$V=\sqrt{u^2+v^2} \quad (3)$$

$$\xi_u=\frac{\sin\alpha}{\sin\alpha_1}\times\frac{1}{2}(P15+P16-P8-P9)-\frac{\sin\alpha}{\sin\alpha_2}\times\frac{1}{2}(P8+P9-P1-P2) \quad (4)$$

$$\xi_v=\frac{1}{2\cos^2\alpha}\times\frac{1}{4}(P6+2P10+P14-P5-2P9-P13-P4-2P8-P12+P3+2P7+P11) \quad (5)$$

$$\xi=\xi_u+\xi_v \quad (6)$$

$$b_1=\arctan(u/v) \quad (7)$$

$$b_2=\arctan(u/v)+180° \quad (8)$$

where u and v represent the zonal and meridional components of the geostrophic wind, respectively. V is the geostrophic wind. ξ_u and ξ_v are the meridional gradient of u and the zonal gradient of v, respectively. ξ is the geostrophic vorticity. P1-P16 are SLP at 16 grid points. α, α_1, and α_2 represent the latitude of the grid points of P8, P12, and P4, respectively. When $v < 0$, b_1 is the geostrophic wind direction. When $v > 0$, b_2 is the geostrophic wind direction.

According to each circulation index and geostrophic wind direction, 27 weather types were classified (Table 1) (You et al., 2024; Liu et al., 2019).

Table 1. Lamb-Jenkinson synoptic circulation classification.

$\lvert\xi\rvert \le V$ (directional types)	$V < \lvert\xi\rvert < 2V$ (hybrid types)	$\lvert\xi\rvert \ge 2V$ (vorticity types)	other
N (north)	AN (anticyclone + north)	A (anticyclone)	UD (undefined)
E (east)	AE (anticyclone + east)	C (cyclone)	
S (south)	AS (anticyclone + south)		
W (west)	AW (anticyclone + west)		
NE (northeast)	ANE (anticyclone + northeast)		
SE (southeast)	ASE (anticyclone + southeast)		
SW (southwest)	ASW (anticyclone + southwest)		
NW (northwest)	ANW (anticyclone + northwest)		
	CN (cyclone + north)		
	CE (cyclone + east)		
	CS (cyclone + south)		
	CW (cyclone + west)		
	CNE (cyclone + northeast)		

https://doi.org/10.5194/egusphere-2026-25
Preprint. Discussion started: 27 February 2026

	CSE (cyclone + southeast)
	CSW (cyclone + southwest)
	CNW (cyclone + northwest)

2.4 HYSPLIT and CWT

The hybrid single particle lagrangian integrated trajectory (HYSPLIT) is a common model for investigating meteorological transmission channels (Chen et al., 2024a; Cheng et al., 2024; Shi et al., 2024). It can efficiently and accurately determine the transport trajectories of different pollutants, and then classify and aggregate the backward trajectories during the study period through the Euler clustering method, and output air mass trajectories with different proportions. In this study, the HYSPLIT model was used to identified backward trajectories of Xinxiang during the period from 2021 to 2023. The model inputs hourly meteorological data from the Global Data Assimilation System (ftp://arlftp.arlhq.noaa.gov/pub/archives/gdas1). Taking the starting point (central location of Xinxiang: 35.30°N, 113.88°E) as a reference, 48-hour backward trajectories terminating at 100 m above ground level were calculated for study period.

Using air mass trajectories, we can interpolate O_3 concentrations and then apply concentration weighted trajectory (CWT) analysis to identify potential source regions and contributions of O_3 in Xinxiang (Shi et al., 2024; Wang et al., 2024). Detailed information is available in Text S1.

3 Results and discussion

3.1 Characteristics of NOI days

3.1.1 Temporal variation of NOI days and NOI occurrence time

Fig. 1 illustrates the monthly variation of NOI days at national monitoring stations in Xinxiang from 2021 to 2023. The DX station recorded the highest cumulative NOI days (470 days), while KF exhibited the lowest frequency (392 days). Additionally, all stations showed similar monthly variation trends: NOI days progressively increased from January to March, peaking in March (42-47 days), maintained high-level fluctuations from April to September (reaching a secondary peak in September (37-48 days)), and declined sharply from October to December, reaching annual minima (15-26 days). This indicated that warm seasons favor NOI occurrence.

https://doi.org/10.5194/egusphere-2026-25
Preprint. Discussion started: 27 February 2026

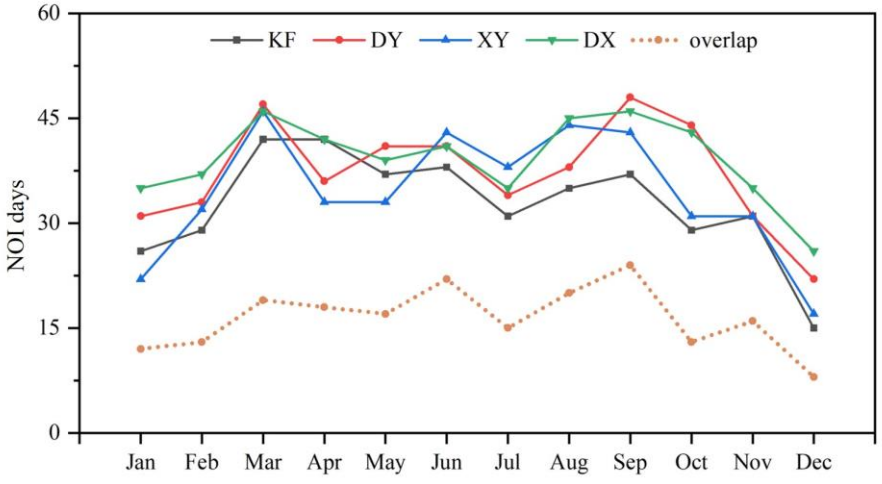

Figure 1: Monthly variation of NOI days at national monitoring stations in Xinxiang, 2021-2023 (overlap: representative NOI days with completely coincident dates across the four stations).

Fig. S3 further demonstrates monthly variations of NOI occurrence time. Type A dominated with 71.35% occurrence frequency across all months, followed by Type B (19.76%) and Type C (8.89%). This indicated that NOI events in Xinxiang tended to occur from 00:00 to 06:00 LT compared with those occurring between 20:00 and 23:00 LT. Notably, Type A generally increased from March to September (69.28-82.67%) compared with other months (60.54-67.50%), while Type B exhibited an opposite trend (Fig. S3). This reflected that warm seasons would intensify the occurrence of Type A.

3.1.2 Impact of NOI occurrence time on O_3 levels

Given the significant temporal variation characteristics of NOI days and NOI occurrence time, different occurrence time of NOI may have potential differential impacts on O_3 levels. Therefore, we further analyzed O_3 diurnal variations of NOI days under different NOI occurrence time in different seasons (Fig. S4). In spring, compared with Type B, Type A exhibited higher initial O_3 concentrations before 12:00 LT but lower afternoon peaks. This difference is likely attributable to lower temperature and solar radiation in Type A (Hu et al., 2021). In other seasons, Type A consistently showed both higher initial O_3 concentrations and peaks than Type B, indicating generally higher O_3 levels in Type A. Moreover, except that Type B and Type C exhibited comparable O_3 levels in spring and summer, Type C displayed higher O_3 concentrations than Type B in other seasons. This indicated that compared with Type A and Type C, Type B exhibited the lowest overall O_3 levels, which also meant that the meteorological conditions of Type B were not conducive to the formation or accumulation of O_3. Overall, the average O_3 concentrations followed: Type A (82.64 μg m^{-3}) > Type C (75.04 μg m^{-3}) > Type B (66.46 μg m^{-3}). We hypothesized that these differences in NOI days may be associated with types of meteorological conditions, as different seasons often featured distinct weather activities, which served as critical factors triggering NOI.

Given the discrepancy in the occurrence dates of NOI days in different stations in Xinxiang, standardizing the dates of local NOI days is essential to investigate the weather type characteristics of NOI days. We established unified occurrence dates

https://doi.org/10.5194/egusphere-2026-25
Preprint. Discussion started: 27 February 2026

through cross-analysis of multi-station data (Fig. S5), and found that KF, XY, DX, and DY had 197 NOI days occurring on the same days during 2021-2023 in Xinxiang. Thus, these 197 NOI days were selected as representatives to characterize the overall occurrence of local NOI days. Notably, the monthly variation characteristics of representative NOI days were highly consistent with those observed at the four stations individually (Fig. 1). This indicated that the representative NOI days could effectively reflect the occurrence of NOI days in Xinxiang and were scientifically valid.

3.2 Weather types of representative NOI days

The Lamb-Jenkinson synoptic circulation classification method was utilized to categorize weather types for representative NOI days. The categorization results are presented in Table S1. 23 weather types were identified from 197 representative NOI days, including 2 vorticity types (named A and C), 8 directional types (including S, SE, SW, W, NW, N, NE and E) and 13 hybrid types (named AE, AN, ANE, ANW, AS, ASE, AW, CE, CN, CS, CSE, CSW and CW). Among them, vorticity types accounted for 46.19% of the total, with anticyclonic type A alone contributing 82 days. Directional and hybrid types accounted for 31.47% and 22.34%, respectively. Fig. S6 displays the mean SLP of representative NOI days under different weather types from 2021 to 2023. It can be seen that the position of high- and low-pressure centers exhibit certain discrepancies among different weather types.

Liu et al. (2019) noted that northern China is frequently affected by large-scale weather systems such as the Yellow River cyclone, the Siberian high, and the Western Pacific subtropical high. These interactions induce frequent shifts in weather classifications and the seasonal migration of high- and low-pressure centers, resulting in distinct monthly meteorological patterns. According to the position of central system and different meteorological elements of each classification, the 23 weather types were classified into four primary weather types: (1) A-type (weather types related with high-pressure), including A, AE, AN, ANE, ANW, AS, ASE and AW; (2) C-type (weather types related with low pressure), including C, CE, CN, CS, CSE, CSW and CW; (3) S-type (geostrophic wind direction to the south), including S, SE and SW; (4) WNE-type (geostrophic wind direction between west-north-east), including W, NW, N, NE and E. Fig. 2 illustrates the proportion of four primary weather types and the days of each weather type. As shown in Fig. 2, representative NOI days predominantly occurred under A-type weather types (113 days, 57.36% of the total), followed by S-type (41 days, 20.81%), C-type (22 days, 11.17%), and WNE-type (21 days, 10.66%). These findings indicated that the meteorological conditions of A-type were most conducive to the occurrence of NOI days.

https://doi.org/10.5194/egusphere-2026-25
Preprint. Discussion started: 27 February 2026

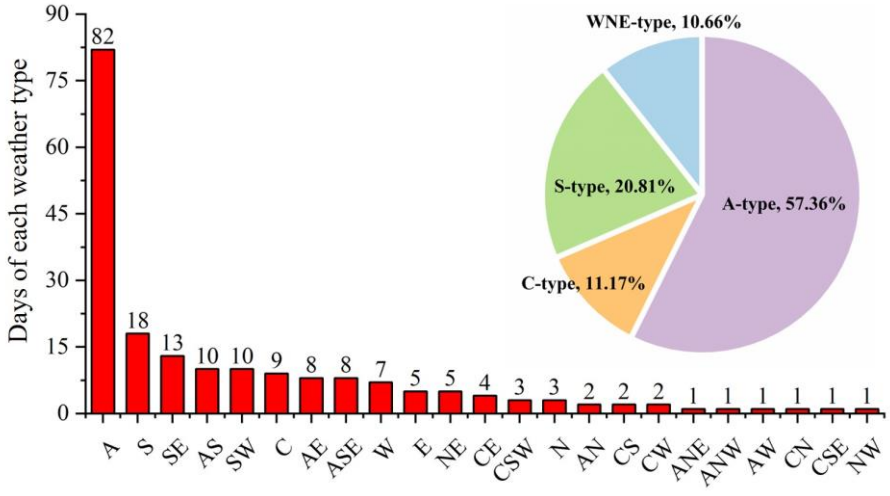

Figure 2: Proportion of four primary weather types and days of each weather type during representative NOI days in Xinxiang, 2021-2023.

Owing to the pronounced differences in meteorological characteristics among seasons in Xinxiang, the occurrence frequencies of various weather types are affected. Thus, we analyzed the seasonal variations of the four primary weather types (Fig. S7). A-type predominantly occurred in autumn (38 days), followed by summer (28 days), winter (24 days), and spring (23 days). Both C-type and S-type exhibited higher frequencies in spring and summer and lower occurrences in autumn and winter. Unlike the other three weather types, WNE-type showed relatively consistent frequencies across seasons, generally 5-6 days. Overall, the four primary weather types exhibited significantly different seasonal variation patterns.

3.3 Meteorological characteristics of primary weather types

The representative NOI days in Xinxiang were classified into four weather types (A-type, C-type, S-type, and WNE-type), with each exhibiting distinct meteorological features. Figs. S8 and 3 illustrate the spatial distributions of SLP and 850 hPa wind fields under four weather types.

https://doi.org/10.5194/egusphere-2026-25
Preprint. Discussion started: 27 February 2026

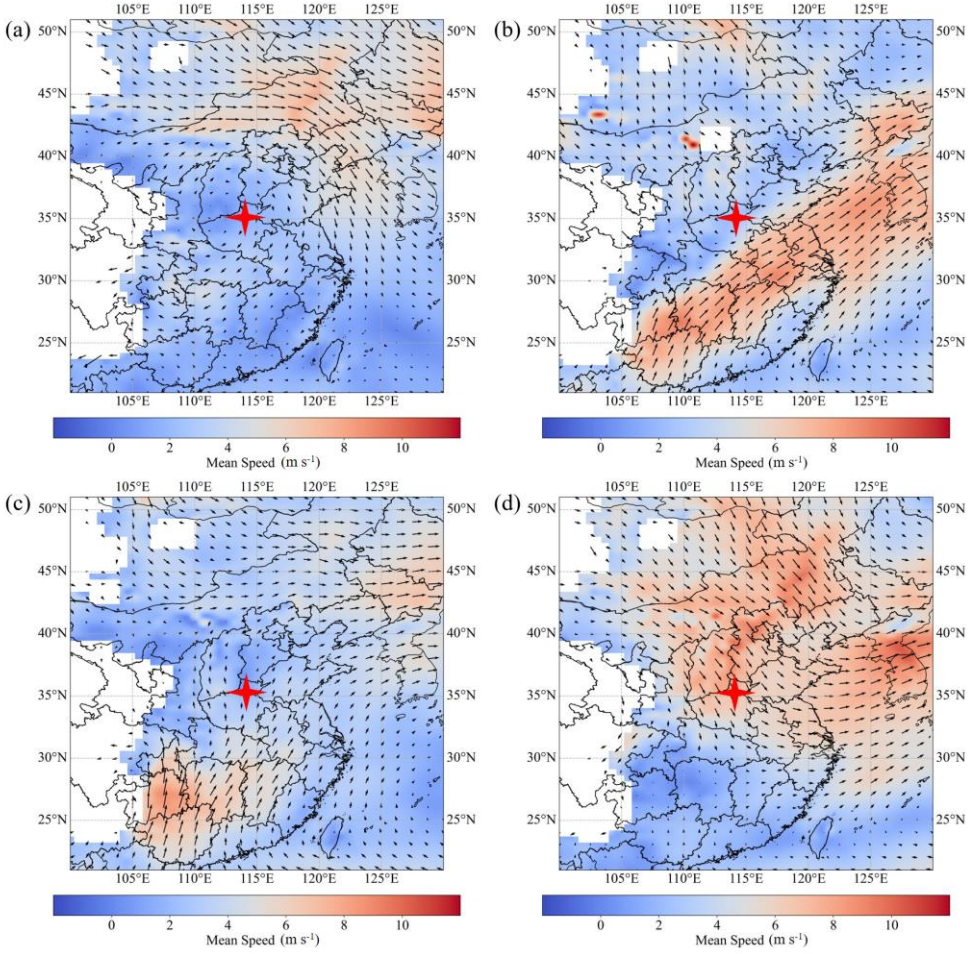

Figure 3: Spatial distribution of wind field at 850hPa under different weather types: (a) A-type, (b) C-type, (c) S-type, (d) WNE-type (asterisk indicates the location of Xinxiang).

Under A-type, Xinxiang was located near a high-pressure center, with an outward-rotating wind field at 850 hPa (Figs. S8(a) and 3(a)), indicating the presence of an anticyclonic high-pressure system. Controlled by this system, surface observations showed the average temperature of 15.53 °C, relative humidity of 64.31%, and wind speed of 2.75 m s^{-1} (Table S2), reflecting a mild, dry, and moderately windy environment. In Section 3.2, we found that A-type occurred most frequently in autumn. Table S3 displays the average temperature, relative humidity, wind speed, wind direction and precipitation observed on the ground in Xinxiang under four weather types in different seasons. In autumn, A-type exhibited the average temperature of 15.71 °C and relative humidity of 65.46%, representing intermediate conditions between the high temperature and humidity of summer and the low temperature and humidity of winter. These moderate conditions favored the stability of the anticyclonic high-pressure system (Holton and Hakim, 2013). Additionally, autumn in northern China was a transitional season with relatively stable atmospheric circulation, influenced by the Siberian high (Chen et al., 2023), which further supported the formation of A-type conditions.

https://doi.org/10.5194/egusphere-2026-25
Preprint. Discussion started: 27 February 2026

In contrast, other seasons presented unfavorable weather conditions for the maintenance of A-type. Summer was characterized by high temperature (23.63 °C) and humidity (73.73%), with vigorous convective activities that easily triggered low-pressure systems (Yihui and Chan, 2005). Winter featured low temperature (5.98 °C), and was often affected by the frequent southward movement of cold air, resulting in rapid changes in weather systems (Zhang et al., 1997b). Spring was marked by unstable atmospheric circulation and frequent frontal activities (Wang et al., 2023c). All these factors hindered the maintenance of high-pressure anticyclones.

Contrasting with A-type, Xinxiang under C-type was dominated by low-pressure systems (Fig. S8(b)). At 850 hPa, a strong airflow originating near the coastal region of Guangxi Province moved continuously northeastward (Fig. 3(b)). This airflow not only moved at a high speed, but also likely carried substantial moisture, significantly enhancing atmospheric instability in its trajectory and surrounding regions (including Xinxiang), intensifying convective activity, and increasing the risk of heavy rainfall. Under the influence of this airflow, Xinxiang experienced significant changes in weather conditions. According to Table S2, the average surface temperature (19.30 °C) and relative humidity (72.43%) under C-type in Xinxiang were higher, and it also had the highest average precipitation (0.49 mm h^{-1}) among the four weather types, which further implied frequent rainfall activities in C-type.

Additionally, C-type primarily occurred in spring and summer, when the East Asian monsoon strengthened. During this period, warm-moist air masses from southern China were transported northward (Yihui and Chan, 2005), supplying abundant moisture to Xinxiang (average relative humidity and precipitation: 72.77%, 0.325 mm h^{-1} in spring and 75.39%, 0.944 mm h^{-1} in summer). The convergence of warm-moist air with cold air facilitated the formation of low-pressure systems (You and Ting, 2021), promoting the occurrence of C-type. Furthermore, high average surface temperatures in spring (20.70 °C) and summer (23.26 °C) enhanced surface heating, atmospheric instability, and convection, providing dynamic conditions for the development of low-pressure systems and the occurrence of heavy rainfall (Yihui and Chan, 2005; Li et al., 2021). Compared with spring and summer, winter was often affected by cold air, with relatively stable atmospheric circulation (Zhang et al., 1997a), low temperature and humidity (8.79 °C and 56.75%, respectively). Although autumn had high humidity level (73.77%), the temperature was low (6.86 °C), and the atmospheric stability was strong, with weaker convective activities (Eom and Myoung-Seok, 2011). These factors were not conducive to the formation and maintenance of low-pressure systems.

Unlike A-type and C-type, S-type and WNE-type were primarily associated with geostrophic wind direction. Under S-type, Xinxiang was located at the junction of the edges between high- and low-pressure (Fig. S8 (c)), indicating that the region was influenced by two different weather systems and thus experienced more frequent weather changes. At 850 hPa, Xinxiang was clearly affected by a southern airflow (Fig. 3(c)), which was consistent with the southern geostrophic wind characteristic of S-type. Ground observations showed that the average wind speed and direction under S-type in Xinxiang were 2.53 m s^{-1} and 136.77 ° (Table S2). The wind direction belonged to the southeast wind, indicating that the surface wind was basically similar to the geostrophic wind.

S-type occurred most frequently in spring and summer, followed by autumn and winter. This seasonal variation resulted from multiple factors. In spring and summer, the northward shift of the Western Pacific subtropical high facilitated collisions

https://doi.org/10.5194/egusphere-2026-25
Preprint. Discussion started: 27 February 2026

between southern warm-moist airflow and cold air masses from the north. This formed frontal convergence zones (high- and low-pressure transition belts) and influenced the southern geostrophic wind in Xinxiang (Yihui and Chan, 2005). During these two seasons, the sun heated the surface, forming a thermal low-pressure area. In coordination with the subtropical high aloft, a vertical pressure gradient with "high-pressure aloft and low-pressure near the surface" was formed (Li et al., 2021). Superimposed with the topography influence of Taihang Mountain, the low-pressure disturbances would be intensified, further contributing to the stable maintenance of the southern geostrophic wind (Xia and Zhang, 2019; Xu and Yao, 2015). Unlike spring and summer, during autumn, the subtropical high retreated southward, and cold air activity increased, significantly shortening the influence duration of transition belts (Eom and Myoung-Seok, 2011). In winter, Xinxiang was controlled by the cold high-pressure system, and the transition belts disappeared (Zhang et al., 1997a). All these factors inhibited the development of the southern geostrophic wind.

Under WNE-type, Xinxiang was controlled by a high-pressure system (Fig. S8(d)). At 850 hPa, the region was obviously influenced by a northwestern airflow (Fig. 3(d)), consistent with the geostrophic wind characteristics of WNE-type. Notably, the average surface wind speed and direction under WNE-type in Xinxiang were 2.78 m s^{-1} and 171.98 ° (Table S2). There was a large deviation between this wind direction and the geostrophic wind, which was mainly attributed to the significant influence of factors such as friction, terrain, and local weather systems on the surface wind (Li et al., 2020a).

Additionally, WNE-type occurred with comparable frequency among all seasons, which was essentially attributable to the combined influence of geographic location, multi-scale circulation systems, and terrain. Xinxiang was situated within the convergence zone where the cold high pressure, the western Pacific subtropical high, and transient migratory ridges interacted (Yihui and Chan, 2005). Although the high-pressure systems dominated in different seasons had various thermal driving mechanisms, they all formed a wind field between the west-north-east direction through the geostrophic balance (Zhang et al., 1997a). Furthermore, the eastern foothills of the Taihang Mountain exerted a stabilizing dynamic influence on local circulation (Xia and Zhang, 2019; Xu and Yao, 2015). The combined effect of weather systems and topographic dynamic forcing ultimately resulted in no significant seasonal differences in the frequency of WNE-type.

3.4 Formation mechanisms of NOI days under different weather types

3.4.1 Regional transport

To explore the triggering factors for the formation of NOI days in Xinxiang under the four different weather types, this study delved deeply into the regional and vertical transport processes. The backward trajectories for Xinxiang under the four weather types are shown in Figs. S9. The spatial distributions of CWT are illustrated in Fig. 4. Under A-type, air masses reaching Xinxiang predominantly originated from the north-northeast direction (64.75%), with a minor contribution from the south-southeast direction (20.91%) (Fig. S9(a)). These two trajectories moved slowly towards Xinxiang. During A-type, the potential source areas of high O_3 levels were mainly distributed in the central and eastern Henan, western Shandong, and northern Anhui (WCWT values: 90-100 μg m^{-3}) (Fig. 4(a)). When the transport trajectories passed over these high-value areas, they carried

https://doi.org/10.5194/egusphere-2026-25
Preprint. Discussion started: 27 February 2026

high-concentration pollutants to the target region. Under C-type, the east direction (46.97%) served as the dominant airflow channel, with short trajectories and slow movement speeds (Fig. S9(b)). This indicated that the pollution transport was mainly influenced by adjacent regions, while the slow movement prolonged the pollutant residence time, increasing the risk of local O_3 accumulation. During this period, the high-value areas of O_3 were concentrated in the central and northern Henan and the border region between Hebei and Shandong (WCWT ≈ 100 μg m^{-3}) (Fig. 4(b)), facilitating the transport of high-concentration O_3 or precursors to Xinxiang.

Influenced by the geostrophic wind, during S-type, the airflow trajectories from the south direction were dominant, contributing 46.34% to the total trajectories (Fig. S9(c)). The high-value areas of O_3 during this period were distributed on both the north and south sides of Xinxiang, with the southern side covering and extending the widest area, mainly including the Central China urban agglomeration (WCWT > 100 μg m^{-3}) (Fig. 4(c)). These O_3 and precursors from southern regions converged and uplifted at the foothills of the Taihang Mountain, exacerbating the local O_3 levels in Xinxiang. Under WNE-type, airflow trajectories were essentially within the W-N-E range (Fig. S9(d)). The potential source regions of high O_3 levels were limited to central and northern Henan, displaying lower WCWT values (70-80 μg m^{-3}) compared with other weather types (Fig. 4(d). This indicated that although WNE-type was influenced by adjacent regions, the overall transport intensity was relatively weak.

https://doi.org/10.5194/egusphere-2026-25
Preprint. Discussion started: 27 February 2026

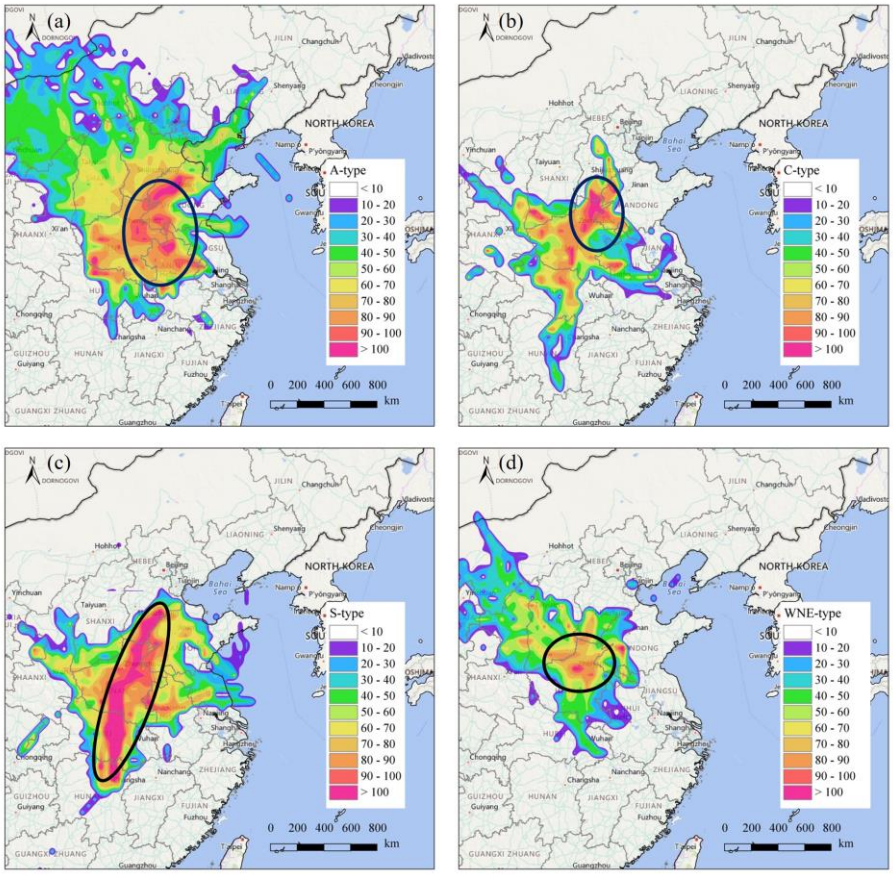

Figure 4: Concentration weighted trajectory (CWT) analysis under different weather types: (a) A-type, (b) C-type, (c) S-type, (d) WNE-type (black circles denote primary high-value areas of O_3).

In summary, the O_3 levels in Xinxiang under four weather types were all affected by regional transport, and mainly exhibited the characteristics of short distances and slow movement speeds.

3.4.2 Vertical transport

Fig. 5 illustrates the pressure vorticity and wind vectors in the vertical profile of Xinxiang. Under A-type, C-type, and WNE-type, there were strong downdrafts in Xinxiang (Fig. 5(a), (b) and (d)). For A-type and WNE-type, the occurrence of downdrafts was primarily associated with high-pressure systems. Although C-type was controlled by a low-pressure system, Xinxiang would be affected by moist airflows during this period, accompanied by frequent heavy rainfall and active atmospheric convection. This easily led to the occurrence of local downdrafts. In contrast, under S-type, Xinxiang was located at the junction of the high-pressure and low-pressure systems. The pressure gradient force drove warm, moist air to rise along the frontal slope, resulting in updrafts (Fig.5(c)). Additionally, the Taihang Mountain to the north of Xinxiang acted as a

https://doi.org/10.5194/egusphere-2026-25
Preprint. Discussion started: 27 February 2026

topography barrier to southern geostrophic winds, enhancing low-level horizontal convergence and forcing vertical uplift of air.

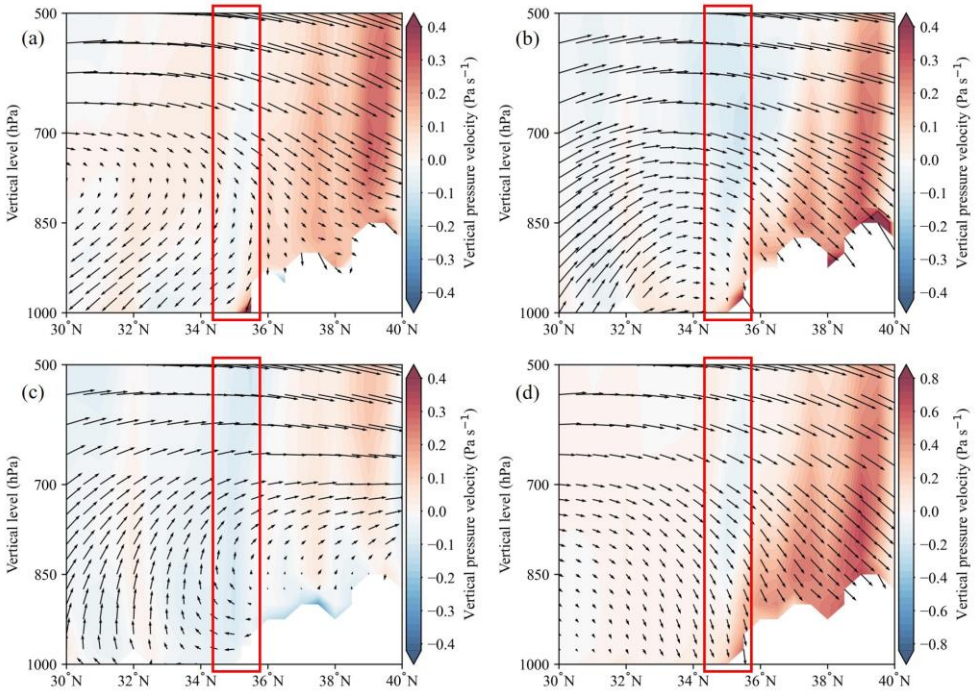

Figure 5: Vertical profiles of pressure vorticity and wind vectors under different weather types: (a) A-type, (b) C-type, (c) S-type, (d) WNE-type (red rectangles indicate the region of Xinxiang).

Fig. S10 presents the vertical profiles of temperature and relative humidity in Xinxiang under four weather types. Under A-type, Xinxiang showed a significant low-level temperature inversion (with a temperature increase of 4.1-4.4 K from 975-950 hPa), which was attributed to the adiabatic compression induced by high-pressure subsidence, leading to the warming of lower-level air (Chen et al., 2022). For relative humidity profiles, we found that during 08:00 and 23:00 LT, mid-level (700-500 hPa) relative humidity remained below 50%, indicating that the subsiding airflow carried dry air (Chen et al., 2022). Although relative humidity displayed an increasing trend from 975 to 850 hPa, likely due to the mixing of subsiding airflow with locally evaporated moisture after reaching the ground (Feng et al., 2022), the pattern of dry air dominance in mid-level persisted. Additionally, CAPE values were extremely low at all times (ranging from 69 to 123 J kg^{-1}), reflecting stable atmospheric stratification with no significant convective potential. This aligned with high-pressure subsidence inhibiting upward motion. Under C-type, a significant temperature inversion layer (temperature increase of 7.6-9.1 K) existed in Xinxiang at 975-950 hPa for all time periods (2:00, 8:00 and 23:00 LT). This temperature inversion resulted from a cold pool mechanism: after heavy rainfall, surface evaporative cooling produced a dense pool of cold air. As this cold pool spread outward, it forced the surrounding warm air to ascend while itself subsiding, thereby forming the inversion layer (Lochbihler et al., 2021). In terms of relative humidity, it was generally dry in mid-level (700-500 hPa), particularly at 02:00 (40.9-45.4%) and 08:00 LT (36.3-

https://doi.org/10.5194/egusphere-2026-25
Preprint. Discussion started: 27 February 2026

44.8%), reflecting entrainment of dry air by downdraft (Feng et al., 2022; Markowski and Richardson, 2011). This period was frequently accompanied by rainfall, with relative humidity increasing at 975-850 hPa (e.g., from 45.5% to 54.2% at 02:00 LT), indicating precipitation evaporation and moist air accumulation in the cold pool. The vertical humidity structure suggested the coexistence of subsidence and convection. In addition, moderate CAPE values (148-265 J kg^{-1}) during this period indicated the presence of convective potential but limited intensity. This likely reflected: (1) Cold pool subsidence after heavy rainfall suppressed further convection, preventing the full release of CAPE (a process known as dissipating convection stage). (2) Local subsidence counteracted a portion of the ascending motion, thus restricting convective development (a process known as mesoscale subsidence suppression).

Under S-type, Xinxiang was situated in the transition zone between high and low pressure, and the frontal slope uplifted warm and moist air, facilitating the development of ascending motion. At 975-900 hPa, relative humidity was generally above 50%, especially at 23:00 LT (56.4-61.1%). This implied that moist air uplift released latent heat, enhancing convective instability (Feng et al., 2022; He and Chen, 2023). Moreover, southern geostrophic winds were blocked by the Taihang Mountain, which enhanced low-level horizontal convergence and forced air to ascend vertically. Moderate CAPE values (217-574 J kg^{-1}) also reflected a certain convective potential, and coupled with frontal lifting, it triggered shallow convection.

WNE-type and A-type had similarities in the vertical effects of high-pressure subsidence, which was mainly manifested in low-level temperature inversion and extremely low CAPE values (69-92 J kg^{-1}). Therefore, no further elaboration is needed here.

Figure S11 shows the vertical profiles of average O_3 concentration under four weather types. We found that high O_3 concentration was mainly distributed between 850 hPa and 1000 hPa, a range that lay primarily within the boundary layer during the daytime. After sunset, the nocturnal residual layer gradually formed, retaining part of the high O_3 concentration from the daytime. Surface O_3 continued to decrease due to processes such as NO titration and dry deposition, resulting in a significant O_3 concentration difference between surface and residual layer. Under A-type and WNE-type, influenced by the systematic subsidence of high-pressure systems, high O_3 concentration in the nocturnal residual layer was easily transported to the surface, leading to the occurrence of NOI events. Under C-type, vertical transport was predominantly driven by the cold pool mechanism, which generated localized subsidence, facilitating the downward transport of O_3 from the nocturnal residual layer to the surface. Under S-type, although upward airflow dominated in Xinxiang, vertical transport still occurred near surface, mainly related to shallow convection. The shallow convection acted as a dynamic driver, enabling the downward transport of O_3 from the nocturnal residual layer and inducing NOI events.

Figure S12 illustrates the diurnal variations of PBLH and U^*. It can be seen that under the four weather types, nocturnal PBLH or U^* showed a fluctuating trend, with the most significant changes in U^*. This further indicated enhanced nocturnal atmospheric instability, which in turn facilitated downward transport processes from the residual layer (He et al., 2022).

https://doi.org/10.5194/egusphere-2026-25
Preprint. Discussion started: 27 February 2026

4 Conclusions

This study systematically investigated the multi-scale synoptic drivers and underlying physical mechanisms governing NOI in a representative city on the North China Plain from 2021 to 2023. A high frequency of 392-470 NOI days was identified, with a distinct seasonal peak during the warm season (March-September). Approximately 71.35% of these events occurred between 00:00 and 06:00 local time, suggesting that the post-midnight period is highly susceptible to episodic perturbations of atmospheric stability, which facilitate the downward intrusion of O_3-rich air from the residual layer to the surface.

Subsequently, based on the Lamb-Jenkinson method, we categorized the synoptic backgrounds into four primary weather types: A-type (57.36%), C-type (11.17%), S-type (20.81%), and WNE-type (10.66%). Among them, A-type exhibited the highest proportion, indicating that its meteorological conditions were most conducive to the formation of NOI days. Furthermore, A-type mainly occurred in autumn; C-type and S-type frequently occurred in spring and summer; WNE-type occurred with comparable frequency across all seasons.

The meteorological characteristics under different weather types varied significantly. A-type was governed by high-pressure anticyclones, with a mild, dry, and moderately windy environment. In autumn, the mild weather conditions, stable atmospheric circulation, and the influence of the Siberian high collectively constituted the primary triggers for the high incidence of A-type. C-type was dominated by low-pressure systems and influenced by moist airflows, resulting in an increased risk of heavy rainfall locally. During C-type, the higher average relative humidity (72.43%) and precipitation (0.49 mm h^{-1}) also demonstrated heavy rainfall. In spring and summer, warm and humid meteorological conditions, active warm-moist airflows, enhanced atmospheric instability, and intensified convective activities collectively contributed to the high occurrence of C-type. S-type occurred within the transition zone between high and low pressure, influenced by southern geostrophic winds. In spring and summer, the high frequency of S-type was driven by the combined effects of the northward shift of the Western Pacific subtropical high, enhanced thermal vertical coupling, and the topography influence. WNE-type was controlled by high-pressure systems, affected by geostrophic winds with W-N-E direction. The unique geographical location, the alternating effects of multi-scale circulation systems, and topography influence together led to comparable occurrence frequency of WNE-type among all seasons.

Under four weather types, the formation of NOI days was influenced by regional transport, which was characterized by short distances and slow movement speeds, exacerbating local O_3 accumulation. Vertical transport of O_3 was driven by distinct triggers under different weather types. Under A-type and WNE-type, the vertical transport was mainly driven by the systematic subsidence of high-pressure systems. C-type was primarily affected by cold pool subsidence airflow. S-type was mainly associated with shallow convection. These processes ultimately transported high O_3 concentration from the nocturnal residual layer to the surface, promoting the occurrence of NOI events.

Overall, our results demonstrate how synoptic-scale circulations modulate nocturnal boundary layer dynamics to trigger NOI. These findings offer an important physical perspective on the nocturnal O_3 budget and provide critical guidance for O_3 forecasting and pollution control in urban environments.

https://doi.org/10.5194/egusphere-2026-25
Preprint. Discussion started: 27 February 2026

Data Availability

The Global Data Assimilation System (GDAS1) dataset from the National Centers for Environmental Prediction (NCEP) is available at ftp:/arlftp.arlhq.noaa.gov/pub/archives/gdas1. The ERA5 reanalysis data can be accessed via https://www.ecmwf.int/en/forecasts/dataset/ecmwf-reanalysis-v5. The MERRA-2 data is obtained from https://gmao.gsfc.nasa.gov/gmao-products/merra-2.

Author contribution

HW and LF designed the research. HW conducted data analysis and simulations, with all co-authors advancing the overall analysis further. HW wrote the paper with support from all co-authors.

Competing interests

The contact author has declared that none of the authors has any competing interests.

Financial support

This work was supported by the Demonstration research project on collaborative prevention and control of fine particulate matter and ozone pollution in Xinxiang (DQGG202133).

References

Bell, B., Hersbach, H., Simmons, A., Berrisford, P., Dahlgren, P., Horányi, A., Muñoz-Sabater, J., Nicolas, J., Radu, R., Schepers, D., Soci, C., Villaume, S., Bidlot, J. R., Haimberger, L., Woollen, J., Buontempo, C., and Thépaut, J. N.: The ERA5 global reanalysis: Preliminary extension to 1950, Q. J. R. Meteorolog. Soc., 147, 4186-4227, https://doi.org/10.1002/qj.4174, 2021.

Chen, L., Chen, W., Hu, P., Chen, S., An, X., Ma, T., and Wang, Z.: Processes and mechanisms of the initial formation of the Siberian High during the autumn-to-winter transition, Clim. Dyn., 62, 315-329, https://doi.org/10.1007/s00382-023-06911-7, 2023.

Chen, T., Guo, J., Tong, B., Cohen, J. B., Chen, X., Yun, Y., Lv, M., Guo, X., and Lee, S. S.: Elucidating the impact of high- and low-pressure systems on temperature inversion from nine years of radiosonde observations in Beijing, Atmos. Res., 271, 106115, https://doi.org/10.1016/j.atmosres.2022.106115, 2022.

Chen, X., Huang, B., Li, M., Xiao, R., Cai, M., Zhou, Z., Ma, S., Gao, W., and Zhou, Z.: A prediction index of the volatile organic compounds pollution conditions in a chemical industrial park based on atmospheric stability, Sci. Total Environ., 919, 170862, https://doi.org/10.1016/j.scitotenv.2024.170862, 2024a.

https://doi.org/10.5194/egusphere-2026-25
Preprint. Discussion started: 27 February 2026

Chen, Z., Liu, R., Wu, S., Xu, J., Wu, Y., and Qi, S.: Diurnal variation characteristics and meteorological causes of autumn ozone in the Pearl River Delta, China, Sci. Total Environ., 908, 168469, https://doi.org/10.1016/j.scitotenv.2023.168469, 2024b.
Cheng, J., Tong, S., Su, H., and Xu, Z.: Association between sub-daily exposure to ambient air pollution and risk of asthma exacerbations in Australian children, Environ. Res., 212, 113556, https://doi.org/10.1016/j.envres.2022.113556, 2022.
Cheng, X., Yu, J., Chen, L., Sun, Y., Zhang, H., Gao, S., Kong, S., Zheng, H., and Wang, H.: Influence of pollution control measures on the reduction of black carbon in an urban site of megacity, Tianjin, China based on ground-monitored and MERRA-2 reanalysis data, Sci. Total Environ., 912, 169466, https://doi.org/10.1016/j.scitotenv.2023.169466, 2024.
Chowdhury, F. I., Arteaga, C., Alam, M. S., Alam, I., and Resco de Dios, V.: Drivers of nocturnal stomatal conductance in C3 and C4 plants, Sci. Total Environ., 814, 151952, https://doi.org/10.1016/j.scitotenv.2021.151952, 2022.
Dong, Y., Li, J., Guo, J., Jiang, Z., Chu, Y., Chang, L., Yang, Y., and Liao, H.: The impact of synoptic patterns on summertime ozone pollution in the North China Plain, Sci. Total Environ., 735, 139559, https://doi.org/10.1016/j.scitotenv.2020.139559, 2020.
Duan, W., Chen, M., Huang, S., Dai, M., Wang, X., and Xu, L.: $PM_{2.5}$ prediction based on Lamb-Jenkinson method and LSTM neural network, Environ. Sci. & Technol., 43, 92-97, https://doi.org/10.19672/j.cnki.1003-6504.2020.01.014, 2020.
Eom, H.-S. and Myoung-Seok, S.: Seasonal and diurnal variations of stability indices and environmental parameters using NCEP FNL data over East Asia, Asia-Pac. J. Atmos. Sci., 47, 181-192, https://doi.org/10.1007/s13143-011-0007-x, 2011.
Feng, X., Wang, S., and Guo, J.: Temperature inversions in the lower troposphere over the Sichuan Basin, China: Seasonal feature and relation with regional atmospheric circulations, Atmos. Res., 271, 106097, https://doi.org/10.1016/j.atmosres.2022.106097, 2022.
Gelaro, R., McCarty, W., Suárez, M. J., Todling, R., Molod, A., Takacs, L., Randles, C. A., Darmenov, A., Bosilovich, M. G., Reichle, R., Wargan, K., Coy, L., Cullather, R., Draper, C., Akella, S., Buchard, V., Conaty, A., da Silva, A. M., Gu, W., Kim, G.-K., Koster, R., Lucchesi, R., Merkova, D., Nielsen, J. E., Partyka, G., Pawson, S., Putman, W., Rienecker, M., Schubert, S. D., Sienkiewicz, M., and Zhao, B.: The modern-era retrospective analysis for research and applications, version 2 (MERRA-2), J. Clim., 30, 5419-5454, https://doi.org/10.1175/JCLI-D-16-0758.1, 2017.
Gilardi, L., Marconcini, M., Metz-Marconcini, A., Esch, T., and Erbertseder, T.: Long-term exposure and health risk assessment from air pollution: impact of regional scale mobility, Int. J. Health Geogr., 22, 11, https://doi.org/10.1186/s12942-023-00333-8, 2023.
He, C., Lu, X., Wang, H., Wang, H., Li, Y., He, G., He, Y., Wang, Y., Zhang, Y., Liu, Y., Fan, Q., and Fan, S.: The unexpected high frequency of nocturnal surface ozone enhancement events over China: characteristics and mechanisms, Atmos. Chem. Phys., 22, 15243-15261, https://doi.org/10.5194/acp-22-15243-2022, 2022.
He, W. and Chen, H.: More extreme-heat occurrences related to humidity in China, Atmos. Oceanic Sci. Lett., 16, 100391, https://doi.org/10.1016/j.aosl.2023.100391, 2023.
He, Y., Wang, H., Wang, H., Xu, X., Li, Y., and Fan, S.: Meteorology and topographic influences on nocturnal ozone increase during the summertime over Shaoguan, China, Atmos. Environ., 256, 118459, https://doi.org/10.1016/j.atmosenv.2021.118459, 2021.
Hersbach, H., Bell, B., Berrisford, P., Hirahara, S., Horányi, A., Muñoz-Sabater, J., Nicolas, J., Peubey, C., Radu, R., Schepers, D., Simmons, A., Soci, C., Abdalla, S., Abellan, X., Balsamo, G., Bechtold, P., Biavati, G., Bidlot, J., Bonavita, M., De Chiara, G., Dahlgren, P., Dee, D., Diamantakis, M., Dragani, R., Flemming, J., Forbes, R., Fuentes, M., Geer, A., Haimberger, L., Healy, S., Hogan, R. J., Hólm, E., Janisková, M., Keeley, S., Laloyaux, P., Lopez, P., Lupu, C., Radnoti, G., de Rosnay, P., Rozum, I., Vamborg, F., Villaume, S., and Thépaut, J. N.: The ERA5 global reanalysis, Q. J. R. Meteorolog. Soc., 146, 1999-2049, https://doi.org/10.1002/qj.3803, 2020.
Holton, J. R. and Hakim, G. J.: An introduction to dynamic meteorology, Academic press2013.
Hoshika, Y., De Carlo, A., Baraldi, R., Neri, L., Carrari, E., Agathokleous, E., Zhang, L., Fares, S., and Paoletti, E.: Ozone-induced impairment of night-time stomatal closure in O_3-sensitive poplar clone is affected by nitrogen but not by phosphorus enrichment, Sci. Total Environ., 692, 713-722, https://doi.org/10.1016/j.scitotenv.2019.07.288, 2019.
Hu, C., Kang, P., Jaffe, D. A., Li, C., Zhang, X., Wu, K., and Zhou, M.: Understanding the impact of meteorology on ozone in 334 cities of China, Atmos. Environ., 248, 118221, https://doi.org/10.1016/j.atmosenv.2021.118221, 2021.

https://doi.org/10.5194/egusphere-2026-25
Preprint. Discussion started: 27 February 2026

Ji, X., Hong, Y., Lin, Y., Xu, K., Chen, G., Liu, T., Xu, L., Li, M., Fan, X., Wang, H., Zhang, H., Chen, Y., Yang, C., Lin, Z., and Chen, J.: Impacts of synoptic patterns and meteorological factors on distribution trends of ozone in Southeast China during 2015–2020, J. Geophys. Res.: Atmos., 128, e2022JD037961, https://doi.org/10.1029/2022JD037961, 2023.

Li, J., Sun, Z., Lenschow, D. H., Zhou, M., Dou, Y., Cheng, Z., Wang, Y., and Li, Q.: A foehn-induced haze front in Beijing: observations and implications, Atmos. Chem. Phys., 20, 15793-15809, https://doi.org/10.5194/acp-20-15793-2020, 2020a.

Li, K., Jacob, D. J., Shen, L., Lu, X., De Smedt, I., and Liao, H.: Increases in surface ozone pollution in China from 2013 to 2019: anthropogenic and meteorological influences, Atmos. Chem. Phys., 20, 11423-11433, https://doi.org/10.5194/acp-20-11423-2020, 2020b.

Li, L., Xie, F., Li, J., Gong, K., Xie, X., Qin, Y., Qin, M., and Hu, J.: Diagnostic analysis of regional ozone pollution in Yangtze River Delta, China: A case study in summer 2020, Sci. Total Environ., 812, 151511, https://doi.org/10.1016/j.scitotenv.2021.151511, 2022a.

Li, X.-B., Yuan, B., Wang, S., Wang, C., Lan, J., Liu, Z., Song, Y., He, X., Huangfu, Y., Pei, C., Cheng, P., Yang, S., Qi, J., Wu, C., Huang, S., You, Y., Chang, M., Zheng, H., Yang, W., Wang, X., and Shao, M.: Variations and sources of volatile organic compounds (VOCs) in urban region: insights from measurements on a tall tower, Atmos. Chem. Phys., 22, 10567-10587, https://doi.org/10.5194/acp-22-10567-2022, 2022b.

Li, Y., Liu, Y., Chen, Y., Chen, B., Zhang, X., Wang, W., Shu, Z., and Huo, Z.: Characteristics of Deep Convective Systems and Initiation during Warm Seasons over China and Its Vicinity, Remote Sens., 13, 4289, https://doi.org/10.3390/rs13214289, 2021.

Liang, D., Yan, H., Tian, Y., Liu, Y., Hao, S., Bai, H., Zhang, G., and Deng, W.: Identification of key controlling factors of ozone pollution in Jinan, northern China over 2013–2020, Front. Ecol. Evol., 10, 930569, https://doi.org/10.3389/fevo.2022.930569, 2022.

Liu, B., Wang, L., Zhang, L., Liao, Z., Wang, Y., Sun, Y., Xin, J., and Hu, B.: Analysis of severe ozone–related human health and weather influence over China in 2019 based on a high-resolution dataset, Environ. Sci. Pollut. Res. Int., 30, 111536-111551, https://doi.org/10.1007/s11356-023-30178-4, 2023.

Liu, J., Wang, L., Li, M., Liao, Z., Sun, Y., Song, T., Gao, W., Wang, Y., Li, Y., Ji, D., Hu, B., Kerminen, V.-M., Wang, Y., and Kulmala, M.: Quantifying the impact of synoptic circulation patterns on ozone variability in northern China from April to October 2013–2017, Atmos. Chem. Phys., 19, 14477-14492, https://doi.org/10.5194/acp-19-14477-2019, 2019.

Liu, N., He, G., Wang, H., He, C., Wang, H., Liu, C., Wang, Y., Wang, H., Li, L., Lu, X., and Fan, S.: Rising frequency of ozone-favorable synoptic weather patterns contributes to 2015–2022 ozone increase in Guangzhou, J. Environ. Sci., 148, 502-514, https://doi.org/10.1016/j.jes.2023.09.024, 2025.

Lochbihler, K., Lenderink, G., and Siebesma, A. P.: Cold Pool Dynamics Shape the Response of Extreme Rainfall Events to Climate Change, J. Adv. Model. Earth Syst., 13, e2020MS002306, https://doi.org/10.1029/2020MS002306, 2021.

Markowski, P. and Richardson, Y.: Mesoscale meteorology in midlatitudes, John Wiley & Sons, https://doi.org/10.1002/9780470682104, 2011.

Molod, A., Takacs, L., Suarez, M., and Bacmeister, J.: Development of the GEOS-5 atmospheric general circulation model: Evolution from MERRA to MERRA2, Geosci. Model Dev., 8, 1339-1356, https://doi.org/10.5194/gmd-8-1339-2015, 2015.

Monks, P. S., Granier, C., Fuzzi, S., Stohl, A., Williams, M. L., Akimoto, H., Amann, M., Baklanov, A., Baltensperger, U., Bey, I., Blake, N., Blake, R. S., Carslaw, K., Cooper, O. R., Dentener, F., Fowler, D., Fragkou, E., Frost, G. J., Generoso, S., Ginoux, P., Grewe, V., Guenther, A., Hansson, H. C., Henne, S., Hjorth, J., Hofzumahaus, A., Huntrieser, H., Isaksen, I. S. A., Jenkin, M. E., Kaiser, J., Kanakidou, M., Klimont, Z., Kulmala, M., Laj, P., Lawrence, M. G., Lee, J. D., Liousse, C., Maione, M., McFiggans, G., Metzger, A., Mieville, A., Moussiopoulos, N., Orlando, J. J., O'Dowd, C. D., Palmer, P. I., Parrish, D. D., Petzold, A., Platt, U., Pöschl, U., Prévôt, A. S. H., Reeves, C. E., Reimann, S., Rudich, Y., Sellegri, K., Steinbrecher, R., Simpson, D., ten Brink, H., Theloke, J., van der Werf, G. R., Vautard, R., Vestreng, V., Vlachokostas, C., and von Glasow, R.: Atmospheric composition change – global and regional air quality, Atmos. Environ., 43, 5268-5350, https://doi.org/10.1016/j.atmosenv.2009.08.021, 2009.

Nair, P. R., Chand, D., Lal, S., Modh, K. S., Naja, M., Parameswaran, K., Ravindran, S., and Venkataramani, S.: Temporal variations in surface ozone at Thumba (8.6°N, 77°E)-a tropical coastal site in India, Atmos. Environ., 36, 603-610, https://doi.org/10.1016/S1352-2310(01)00527-1, 2002.

Paoletti, E.: Ozone and Mediterranean ecology: plants, people, problems, Environ. Pollut., 157, 1397-1398, https://doi.org/10.1016/j.envpol.2009.03.001, 2009.

Sánchez, M. L., De Torre, B., García, M. A., and Pérez, I.: Ozone concentrations at a high altitude station in the Central Massif (Spain), Chemosphere, 60, 576-584, https://doi.org/10.1016/j.chemosphere.2004.12.079, 2005.
Shen, L., Diao, Y., Zhao, T., Gu, X., and Shi, S. S.: Meteorological influence on persistent O_3 pollution events in Wuxi in the Yangtze River Delta, China, Sci. Total Environ., 917, 170484, https://doi.org/10.1016/j.scitotenv.2024.170484, 2024.
Shi, J., Wu, X., Han, X., Zhong, Y., Wang, Z., and Ning, P.: Characterization and sources of carbonaceous aerosols in southwest plateau of China: Effects of biomass burning and low oxygen concentration, Atmos. Environ., 318, 120250, https://doi.org/10.1016/j.atmosenv.2023.120250, 2024.
Song, A., Yan, Y., Kong, S., Ma, J., and Tong, Z.: Impact of synoptic climate system interaction on surface ozone in China during 1950–2014, Atmos. Environ., 279, 119126, https://doi.org/10.1016/j.atmosenv.2022.119126, 2022.
Wang, D., Zhou, J., Han, L., Tian, W., Wang, C., Li, Y., and Chen, J.: Source apportionment of VOCs and ozone formation potential and transport in Chengdu, China, Atmos. Pollut. Res., 14, 101730, https://doi.org/10.1016/j.apr.2023.101730, 2023a.
Wang, G., Liu, X., Kong, F., Zhu, Z., Yan, P., Gao, W., and Zhao, N.: Characteristics of fine particulate matter in Linyi during the 24th Olympic winter Games: An insight into the components, sources, transport pathways, and source distribution, Atmos. Pollut. Res., 15, 102034, https://doi.org/10.1016/j.apr.2023.102034, 2024.
Wang, H., Fan, L., Deng, X., Huang, H., and Ye, D.: Research on the characteristics and triggering factors of concurrent events of ozone pollution and nocturnal ozone increase in Xinxiang, China, Atmos. Environ., 361, 121494, https://doi.org/10.1016/j.atmosenv.2025.121494, 2025.
Wang, H., Wang, H., Lu, X., Lu, K., Zhang, L., Tham, Y. J., Shi, Z., Aikin, K., Fan, S., Brown, S. S., and Zhang, Y.: Increased night-time oxidation over China despite widespread decrease across the globe, Nat. Geosci., 16, 217-223, https://doi.org/10.1038/s41561-022-01122-x, 2023b.
Wang, J., Chen, L., and Li, S.: Characteristics of spring Mongolian cyclones in the recent 70 years: Background circulations and weather influences, Int. J. Climatol., 44, 328-343, https://doi.org/10.1002/joc.8342, 2023c.
Wang, K., Xie, F., Sulaymon, I. D., Gong, K., Li, N., Li, J., and Hu, J.: Understanding the nocturnal ozone increase in Nanjing, China: Insights from observations and numerical simulations, Sci. Total Environ., 859, 160211, https://doi.org/10.1016/j.scitotenv.2022.160211, 2023d.
Wang, Y., Liu, R., and Xin, F.: Impact of atmospheric circulation patterns on ozone changes in the Pearl River Delta from 2015 to 2020, Environ. Sci., 44, 3080-3088, https://doi.org/10.13227/j.hjkx.202206106, 2023e.
Wu, J., Li, C., Ma, Z., Sun, Z., Zhu, X., and Dong, F.: Influence of meteorological conditions on ozone pollution at Shangdianzi station based on weather classification, Environ. Sci., 41, 4864-4873, https://doi.org/10.13227/j.hjkx.202003307, 2020.
Wu, Y., Chen, W., You, Y., Xie, Q., Jia, S., and Wang, X.: Quantitative impacts of vertical transport on the long-term trend of nocturnal ozone increase over the Pearl River Delta region during 2006–2019, Atmos. Chem. Phys., 23, 453-469, https://doi.org/10.5194/acp-23-453-2023, 2023.
Xia, R. and Zhang, D.-L.: An Observational Analysis of Three Extreme Rainfall Episodes of 19–20 July 2016 along the Taihang Mountains in North China, Mon. Weather Rev., 147, 4199-4220, https://doi.org/10.1175/mwr-d-18-0402.1, 2019.
Xu, H. and Yao, W.: A Numerical Study of the Beijing Extreme Rainfall of 21 July 2012 and the Impact of Topography, Adv. Meteorol., 2015, 980747, https://doi.org/10.1155/2015/980747, 2015.
Xu, J., Huang, X., Wang, N., Li, Y., and Ding, A.: Understanding ozone pollution in the Yangtze River Delta of eastern China from the perspective of diurnal cycles, Sci. Total Environ., 752, 141928, https://doi.org/10.1016/j.scitotenv.2020.141928, 2021.
Xue, Y., Wang, L., Jing, Y., Zhang, T., He, S., Ho, K. F., Huang, Y., Chen, L., Cui, L., and Cao, J.: Asian monsoon and local valley wind caused transport of volatile organic compounds episode across Qinling Mountain in China, J. Geophys. Res.: Atmos., 128, e2022JD038256, https://doi.org/10.1029/2022JD038256, 2023.
Yihui, D. and Chan, J. C. L.: The East Asian summer monsoon: an overview, Meteorol. Atmos. Phys., 89, 117-142, https://doi.org/10.1007/s00703-005-0125-z, 2005.
You, Y. and Ting, M.: Low Pressure Systems and Extreme Precipitation in Southeast and East Asian Monsoon Regions, J. Clim., 34, 1147-1162, https://doi.org/10.1175/jcli-d-20-0206.1, 2021.
You, Y., Wang, X., Wu, Y., Chen, W., Chen, B., and Chang, M.: Quantified the influence of different synoptic weather patterns on the transport and local production processes of O_3 events in Pearl River Delta, China, Sci. Total Environ., 912, 169066, https://doi.org/10.1016/j.scitotenv.2023.169066, 2024.

https://doi.org/10.5194/egusphere-2026-25
Preprint. Discussion started: 27 February 2026

Zhang, Y., Sperber, K. R., and Boyle, J. S.: Climatology and interannual variation of the East Asian winter monsoon: Results from the 1979–95 NCEP/NCAR reanalysis, Mon. Weather Rev., 125, 2605-2619, https://doi.org/10.1175/1520-0493(1997)125<2605:CAIVOT>2.0.CO;2, 1997a.

Zhang, Y., Li, J., Li, J., Pan, X., Wang, W., Zhu, L., Wang, Z., Chen, X., Yang, W., and Wang, Z.: An intercomparison of ozone taken from the Copernicus atmosphere monitoring service and the second Modern-Era retrospective analysis for research and applications over China during 2018 and 2019, J. Environ. Sci., 114, 514-525, https://doi.org/10.1016/j.jes.2022.01.045, 2022.

Zhang, Y., Sperber, K., Boyle, J., Dix, M., Ferranti, L., Kitoh, A., Lau, K., Miyakoda, K., Randall, D., Takacs, L., and Wetherald, R.: East Asian winter monsoon: results from eight AMIP models, Clim. Dyn., 13, 797-820, https://doi.org/10.1007/s003820050198, 1997b.

Zhao, Y., An, X., Sun, Z., Li, Y., and Hou, Q.: Identification of health effects of complex air pollution in China, Int. J. Environ. Res. Public Health., 19, 12652, https://doi.org/10.3390/ijerph191912652, 2022.

Zhou, M., Zeng, Y., Li, J., Zhou, Y., Zhu, D., Luo, C., Zhuang, Y., Zhang, C., Wang, B., and Situ, S.: lmpact of atmospheric circulation patterns and volatile organic compounds on ozone pollution in Foshan City, Guangdong Province, Acta Sci. Circumst., 43, 215-225, https://doi.org/10.13671/j.hjkxxb.2023.0121, 2023.

Zhu, L., Han, X., Xu, L., Guan, X., Gong, A., Liu, H., and Zhang, M.: Nocturnal ozone enhancement in Shandong Province, China, in 2020–2022: Spatiotemporal distribution and formation mechanisms, Sci. Total Environ., 925, 171542, https://doi.org/10.1016/j.scitotenv.2024.171542, 2024.

Zhu, X., Ma, Z., Li, Z., Wu, J., Guo, H., Yin, X., Ma, X., and Qiao, L.: Impacts of meteorological conditions on nocturnal surface ozone enhancement during the summertime in Beijing, Atmos. Environ., 225, 117368, https://doi.org/10.1016/j.atmosenv.2020.117368, 2020.

Zhu, Y., Chen, D., Li, W., and Zhang, P.: Lamb-Jenkinson circulation type classification system and its application in China, J. Nanjing Inst. Meteor., 30, 289-297, https://doi.org/10.13878/j.cnki.dqkxxb.2007.03.001, 2007.